Electromagnetic ion cyclotron wave fields in a realistic dipole field

R. E. Denton [1]

[1]Department of Physics and Astronomy, Dartmouth College, Hanover, New Hampshire, USA

Key Points:

- The latitudinal evolution of the frequency and wave vector spectrum of simulated electromagnetic ion cyclotron waves is described.
- During propagation, the waves grow and the wave vector broadens and turns radially outward leading to linear polarization.
- When waves propagate to high latitude, the parallel wave vector decreases, but frequency filtering can limit this effect.

Corresponding author: R. E. Denton, `redenton at dartmouth.edu`

Abstract

We describe in detail simulated electromagnetic ion cyclotron (EMIC) waves generated self consistently in a dipole magnetic field for a plasmasphere or plume-like plasma at geostationary orbit consisting of cold H+, He+, and O+, and hot protons with temperature anisotropy $A = T_{\perp,\mathrm{hot}}/T_{\|,\mathrm{hot}} = 1$ at the magnetic equator on the central field line of the simulation. Here we concentrate predominantly on the latitudinal variation of the waves. The waves grow as they propagate away from the magnetic equator to higher latitude while the wave vector turns outward radially and the polarization becomes linear. We calculate the detailed wave spectrum in four latitudinal ranges varying from magnetic latitude MLAT close to 0° (magnetic equator) up to 21°. The strongest waves are propagating away from the magnetic equator, but some wave power propagating toward the magnetic equator is observed due to local generation (especially close to the magnetic equator) or reflection. The He band waves, which are generated relatively high up on their dispersion surface, are able to propagate all the way to MLAT = 21°, but the H band waves experience frequency filtering, with no equatorial waves propagating to MLAT = 21° and only the higher frequency waves propagating to MLAT = 14°. The result is that the wave power averaged $k_\|$ for the He waves scales like the inverse of the local magnetic field, whereas that for the H band waves is almost constant. While the perpendicular wave vector turns outward, it broadens. These wave fields should be useful for simulations of radiation belt particle dynamics. In this case, the lowest minimum resonant energies of relativistic electrons will be for interaction with the higher frequency H band waves.

1 Introduction

In order to quantitatively understand relativistic electron variability, it is essential to understand both acceleration and loss mechanisms [*Summers et al.*, 2007; *Shprits et al.*, 2008]. Electromagnetic Ion Cyclotron (EMIC) waves are thought to be a major loss mechanism for relativistic electrons, especially in the dusk local time sector [*Millan and Thorne*, 2007]. *Fraser et al.* [2006] give a brief review of EMIC waves.

Considering a plasma consisting of H+, He+, and O+ ions, EMIC waves can occur in three wave bands [*Andre*, 1985; *Hu et al.*, 2010]. The H band, He band, and O band waves asymptote respectively to the H+ gyrofrequency, the He+ gyrofrequency, and the O+ gyrofrequency at large values of the component of the wave vector parallel to the background magnetic field, $k_\|$. At parallel propagation ($k_\perp = 0$), as $k_\|$ decreases, the H band frequency decreases to a cutoff ($k_\| = 0$) frequency above the He+ gyrofrequency, and the He band frequency extends down to a cutoff frequency above the O+ gyrofrequency [*Andre*, 1985]. The O band is unique in that it extends down to zero frequency for $k_\| = 0$.

The topology of the H and He band wave surfaces can be different, however, for finite $k_\perp$. For a cold plasma and at finite wave normal angle θ_{kB} between the wave vector **k** and the magnetic field **B**, the wave surfaces for parallel propagation split into parts that interconnect. For instance, as the frequency decreases for nearly parallel propagation ($k_\perp \ll k_\|$) on the high frequency part of the H or He band waves, there is a crossover frequency at which the left-hand polarized surface joins on to a right hand polarized surface. Also, for both of these modes there is a bi-ion resonance at large $k_\perp$, above the He+ gyrofrequency for the H band or above the O+ gyrofrequency for the He band. The resulting topology is quite complex; see the descriptions by *Andre* [1985] and *Hu et al.* [2010], and especially by *Hu* [2010].

But the cold plasma dispersion relations may not be applicable to the simulation described in this paper. *Denton et al.* [2014] showed that when a hot component of protons was present, the left hand polarized surfaces at parallel propagation continued to maintain their topological integrity to quite large $k_\perp$. The right hand polarized wave surfaces were heavily damped where they came close to crossing the left hand polarized surfaces. In this case, the wave surfaces are similar to those at parallel propagation and the lower frequency limit of the left-hand polarized waves continues to be the cutoff ($k_{\parallel} = 0$) frequency for that wave band. Regardless of these considerations, as $k_{\perp}$ becomes comparable to $k_{\parallel}$, the waves become more electrostatic and the polarization shifts toward linear polarization on all wave surfaces.

EMIC waves are usually most unstable in the vicinity of the magnetic equator where the anisotropy and plasma beta are largest [*Hu and Denton*, 2009; *Hu et al.*, 2010]. The unstable region of each wave dispersion surface is on the left hand polarized part of the surface where the frequency has a significant slope with respect to $k_{\parallel}$ and is not too close to a gyrofrequency. The group velocity of EMIC waves is approximately along the magnetic field, so EMIC wave energy propagates along the magnetic field away from the magnetic equator toward the ionosphere. As the waves propagate toward the ionosphere, the wave frequency remains constant, but the gyrofrequencies of the various ion species increase due to the increasing magnetic field. Because of this, the wave frequency normalized to the gyrofrequency decreases. If the waves stay on the left hand polarized surface as they propagate toward the ionosphere, they would remain left hand polarized or become linearly polarized as they refract outward [*Hu and Denton*, 2009; *Hu et al.*, 2010]. Then they might reflect at their cutoff frequency . But there is also the possibility of tunneling to the right hand polarized surface near the crossover frequency or to lower wave bands near the cutoff frequency [*Johnson and Cheng*, 1999].

To date, the EMIC wave fields used to calculate effects on relativistic particles have been found either from models [*Omura and Zhao*, 2012, 2013; *Kubota et al.*, 2015] or simulations in straight coordinates [*Liu et al.*, 2010a,b]. But *Denton et al.* [2014] recently showed that it was possible to do full scale EMIC waves simulations in dipole field geometry in a meridional plane. Here we use the same simulation code to calculate realistic two-dimensional wave fields and then examine their properties. Denton et al.'s emphasis was on the radial structure of the waves and the effects of differing composition. Here we concentrate on the latitudinal variation of the wave fields. A crucial factor affecting this variation is the geometry of the Earth's dipole magnetic field. The curvature of the field leads to refraction, and the varying magnetic field strength leads to motion of wave packets along the normalized dispersion surfaces.

A description of the simulation follows in section 2; the simulated wave fields are described in section 3; and a summary follows in section 4.

2 Simulation of wave fields

The hybrid code was described in detail by *Hu and Denton* [2009] and *Hu et al.* [2010]. Particles are used for the ions, while the electrons are described by an inertialess fluid. The plasma is quasi-neutral, so the electron density is equal to the ion density. The magnetic field is advanced using Faraday's law. The electric field is found from $\mathbf{E} = -\mathbf{u}_e \times \mathbf{B} + \eta \mathbf{J}$, where $\mathbf{B}$ is the magnetic field, $\mathbf{J} = \nabla \times \mathbf{B}/\mu_0$ (Ampere's law), $\mathbf{u}_e$ is the electron velocity found using $\mathbf{J} = \mathbf{J}_i - en_e\mathbf{u}_e$, $\mathbf{J}_i$ is the ion current density, n_e is the electron density, and μ_0 is the vacuum permeability. The resistivity η is nonzero only near the boundaries, where it damps the waves [*Hu and Denton*, 2009]; other than at these boundary regions, the parallel electric field is zero. Therefore one limitation of our simulation is that there is no electron Landau damping. Landau damping would cause a reduction in obliquely propagating waves, that is, waves with wave vector not parallel to $\mathbf{B}$, especially in the later parts of the simulation.

The hybrid code uses generalized orthogonal coordinates [*Arfken*, 1970], and here we employ dipole coordinates. The inner and outer L shell boundaries are along dipole field lines. But the background magnetic field in the interior of the simulation domain is not exactly exactly dipolar. The initial magnetic field was derived from an anisotropic MHD simulation to get a near-equilibrium initial state [*Hu et al.*, 2010]; but the initial

Table 1. Simulation Parameters at the normalization point, $(q, r) = (0,1)$

Species s	N_s (cm^{-3})	$T_{\parallel s}$ (keV)	$\beta_{\parallel s}$	$\frac{T_{\perp s}}{T_{\parallel s}}$	p_s [a]	$\frac{\text{particles}}{\text{cell}}$
Hot H+	1	10	0.403	2	6	8192
Cold H+	27.6	0.002	0.002	1	4	256
Cold He+	0.9	0.002	7×10^{-5}	1	4	256
Cold O+	0.5	0.002	4×10^{-5}	1	4	256
Cold e-	30	0	0	NA	$N_e = N_{ion}$	NA

[a] The density of each species varies across field lines like L^{-p_s}.

state is still not a true equilibrium, and in this case, there are initially some small amplitude large-scale oscillations, most clearly seen in the parallel fluctuations (not shown in this paper, but included in the data sets). Once the EMIC waves grow to large amplitude, however, they totally dominate the wave power.

The simulations are two dimensional representing a meridional plane. Only the northern half of this plane is simulated; symmetry conditions are used at the magnetic equator. The first coordinate q varies along the dipole magnetic field with value 0 at the magnetic equator and a value of 1 at our ionospheric boundary. The ionospheric boundary is at a magnetic latitude MLAT of 47° for the central L shell in the simulation. This range of latitude is large enough that the waves have passed through all relevant resonant surfaces before they reach the ionospheric boundary where they are damped. The q coordinate is chosen so that equal spacing in q corresponds to a distance in real space proportional to B along the central L shell in the simulation. (Since the coordinates are orthogonal, surfaces of constant q are also surfaces of the usual dipole coordinate that is orthogonal to L. There is freedom to choose a particular mapping between q and distance only at one particular L shell.) Since flux tubes have area $\propto 1/B$, the volume of each cell in the simulation is exactly constant along the central field line and roughly constant at other L values; this is a good choice for simulation of Alfvén waves, and leads to a relatively even distribution of particles, which is good for keeping the numerical noise low. The second coordinate in our simulation is the normalized dipole L value, $r = L/L_0$, where $L_0 = 6.6$ is the central L shell. We use a range of r of 0.96 to 1.04, corresponding to L varying from $L_1 = 6.34$ to $L_2 = 6.86$. The third coordinate is s, which is in the azimuthal direction eastward.

We assume a plasmasphere or plasmaplume-like plasma with $N_e = 30$ cm^{-3}. In Table 1, we list the run parameters at the normalization point, which is at the middle r value ($r = 1$) at the magnetic equator ($q = 0$). The parallel plasma beta of the hot H+, $\beta_{\parallel hot} \equiv N_{hot} T_{\parallel hot}/(B^2/(2\mu_0)) = 0.403$, where N_s is the species density, $T_{\parallel s}$ is the species temperature parallel to the magnetic field, and μ_0 is the vacuum permeability. With $T_{\perp hot}/T_{\parallel hot} = 2$, the plasma is very unstable, although not beyond the range of realistic conditions. Our ion inertial scale length, $d_i \equiv c/\omega_{pi} = 41.4$ km = 0.00652 R_E, where c is the speed of light, the ion plasma frequency (using the total ion density) is $\omega_{pi} \equiv \sqrt{N_e e^2/m_p \epsilon_0}$, e is the elementary charge m_p is the proton charge, and ϵ_0 is the vacuum permittivity. The simulation is full scale; that is, the ratio of the simulation d_i to R_E is realistic. We used 769 grid points along the dipole magnetic field (q direction) and 97 across the magnetic field (r direction). These values were chosen in order to well resolve the relevant spatial scales. There are about 25 grid points per dominant parallel wavelength at the magnetic equator, and these waves are also resolved at higher latitude. At the central L shell, there were about 4 grid points per thermal gyroradius of the hot protons. In order to achieve low simulation noise, we used 8192 particles per grid point to simulate the ring current H+ and 256 particles per grid point to simulate each of the three remaining particle populations, cold H+, cold He+, and cold O+.

In the initialization, $T_{\rm hot} \equiv 2T_{\perp \rm hot}/3 + T_{\| \rm hot}/3$ was set to be constant across L shells (flux surfaces), but N_s varied like L^{-p_s}, with the power law coefficients p_s equal to 4 for the cold species, and 6 for the hot protons. The L^{-4} dependence for cold species is typical in the outer magnetosphere, whereas L^{-6} for the hot density combined with constant $T_{\rm hot}$ and $B \approx L^{-3}$ means that $\beta_{\rm hot} \equiv N_{\rm hot}T_{\rm hot}/(B^2/(2\mu_0))$ was roughly constant across L shells [*Lui et al.*, 1987]. The hot H+ anisotropy $A_{\rm hot} \equiv T_{\perp \rm hot}/T_{\| \rm hot} - 1$ was set to $2\cos((\pi/2)(L - L_0)/(L_2 - L_0))$ at the magnetic equator, which means that the plasma was unstable in the middle L shall region of the simulation domain, but was stable near the L boundaries, where $A_{\rm hot} = 0$. Along the field lines, the density and temperature of the cold species was constant, but the density and temperatures of the hot protons varied along the field lines in accordance with anisotropic equilibrium [*Hu and Denton*, 2009].

A major goal of deriving these simulation fields is to use them in test particle simulations of radiation belt particle dynamics. Because of this, we didn't want any wave power at grid scales, which are not accurately described in a finite difference simulation. We ran our simulation using spatial smoothing at each time step (a 0.25/0.5/0.25 averaging stencil [*Birdsall and Langdon*, 1985] applied in each direction to the electric field, the ion current density, and the ion charge density in a way that preserves energy conservation). Finally, in order to entirely eliminate grid scale structure, we filtered the electric and magnetic fields of the saved data in Fourier space, zeroing out modes with wave number greater than half the maximum (Nyquist) value in each direction. (This filtering is not energy conserving, but is only applied to the wave fields after the simulation is finished.)

3 Simulation wave fields

The wave fields grow spontaneously from the simulation noise. In Figure 1, we show the wave magnetic field at four times, t = 50 s, 70 s, 90 s, and 110 s. The roughly horizontal green curves in each panel are at MLAT = 10° (lowest curve), 20°, 30°, and 40° (highest curve). The central nearly vertical green curve in each panel is the equilibrium flux surface connecting to the normalization point at $q = 0$; this is not exactly dipolar, which would be a vertical line in the plot. The L component in Figure 1a (first column) is perpendicular to the equilibrium flux surfaces rather than being strictly in the dipole r direction; positive s component is into the page. At each time, the equilibrium field is found by averaging the field between a time 10 s earlier and a time 10 s later. Then the instantaneous perturbed field $d\mathbf{B}$ is found at the times indicated by subtracting that equilibrium field.

The waves grow at early times (see Figure 1A, the bottom panels) in the middle region of L, where $A_{\rm hot}$ peaks, and close to the magnetic equator, where $\beta_{\| \rm hot}$ is largest. (The magnetic field increases at large q toward the ionospheric boundary. Also, in anisotropic equilibrium, the hot density and anisotropy decrease at large q.) The waves do not grow exactly at the magnetic equator ($q = 0$) because of the symmetry boundary condition, which causes the wave fields to be zero there. At later times (upper panels in Figure 1), the wave fields have propagated upward close to the ionospheric boundary ($q = 1$).

Close to the equator, dB_L is nearly equal to dB_s, which would be expected for parallel propagating waves with circular polarization. Near $q = 1$, however, the azimuthal component, dB_s, is larger than the L shell component, dB_L, as expected for waves that are becoming more linearly polarized. (Because of Faraday's law, and the fact that the gradients are only in the meridional plane, dB_s is larger than dB_L, which is usually the case also for observations.) Note also that the wave patterns of dB_L (Figure 1a) have wave vector that is much closer to being parallel (nearly horizontal wave fronts) than those of dB_s (Figure 1b).

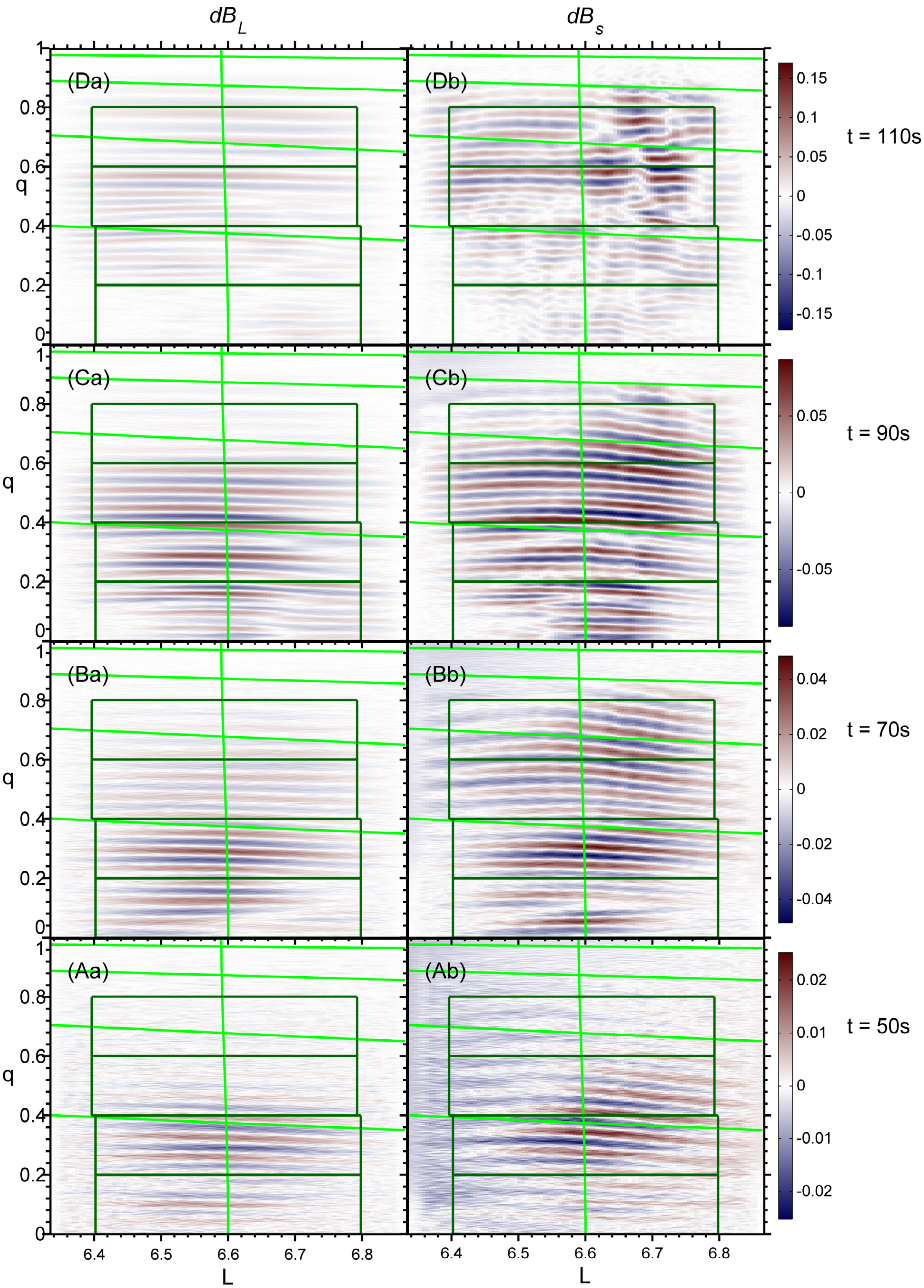

Figure 1. Left column (a) Component of wave magnetic field in the L direction perpendicular to the flux surfaces, dB_L, and right column (b) azimuthal component, dB_s, positive into the page, at the four times listed on the right side of the figure. The roughly horizontal green curves are at MLAT = 10° (lowest curve), 20°, 30°, and 40° (highest curve), while the nearly vertical green curve is the central equilibrium flux surface. The black boxes enclose regions used for Fourier analysis, as described in the text.

The interference patterns in Figure 1Db suggest that there is considerable reflection of waves at $t = 110$ s [see *Hu et al.*, 2010], and that the reflected waves are significantly oblique, leading to interference dominantly for dB_s rather than dB_L. Note that the resistive layer (section 2) is only between $q = 0.97$ and 1, so the observed reflection, strongest between $q = 0.8$ and 0.9 (Figure 1Db), must be occurring at the natural frequency for the dominant He wave band, presumably the cutoff frequency.

3.1 Frequency distribution

Figure 2 shows the wave power of transverse waves versus frequency for time intervals of 20 s centered on the times used for Figure 1. Before calculating the frequency spectrum, the data were windowed in time using a Welch data window [*Press et al.*, 1986]. The wave components dB_L and dB_s were combined into a complex transverse field with the frequency defined such that positive frequency represents right hand polarized waves (right hand rotation around the magnetic field direction), whereas negative frequency represents left hand polarized waves [*Kodera et al.*, 1977]. The waves near the magnetic equator (Figure 2A) are dominantly left hand polarized (negative frequency), although there is some mixture of left and right hand polarization. But at the largest range of q centered on $q = 0.7$, the wave power in the negative and positive frequencies is almost equal, indicating linear polarization.

The gray vertical lines in Figure 2 are at the O+ and He+ gyrofrequencies, 1/16 and 1/4 the proton gyrofrequency, respectively. The wave power at zero frequency is an artifact of how the power spectrum is calculated, and can be ignored. There is very little if any wave power in the O+ EMIC wave band below the O+ gyrofrequency (between the two innermost vertical gray lines). That is consistent with the fact that the linear growth rate for the O+ mode is small. The first time interval for which the power spectrum is calculated is for $t = 40$–60 s, plotted as the dotted black curves. The dominant early wave growth is in the He+ EMIC waveband between $|\omega/\Omega_{\rm cp}| = 1/16$ and 1/4. At $q = 0.1$, close to the magnetic equator, the peak in wave power drops sharply at the upper frequency limit for the He+ band, $|\omega/\Omega_{\rm cp}| = 1/4$. At larger q values, the He+ mode peak in wave power overlaps $|\omega/\Omega_{\rm cp}| = 1/4$, suggesting that there is some wave growth at the higher latitudes. This is because the frequency of waves is constant as they propagate along the magnetic field line. So if the waves had simply propagated from near the magnetic equator, there would also be a steep drop in wave power at $|\omega/\Omega_{\rm cp}| = 1/4$ at the larger q values. Note that our normalization is to the proton gyrofrequency at the magnetic equator ($q = 0$), and the normalized frequency at higher q would be lower if the local gyrofrequency were used for the normalization. Thus it appears that the waves at $|\omega/\Omega_{\rm cp}| = 1/4$ are generated locally at larger q where the locally normalized wave frequency is lower. At later times (progressing from the blue to green to red curves), there is also wave growth in the H EMIC wave band at frequencies above $|\omega/\Omega_{\rm cp}| = 1/4$.

Note the progression of wave power along the field line away from the magnetic equator. The He band wave power in Figure 2A ($q = 0.1$) and Figure 2B ($q = 0.3$) reaches its highest values for the last three time intervals (blue, green, and red curves); but in Figure 2C ($q = 0.5$), the maximum He band wave power occurs only for the last two time intervals (green and red curves); and in Figure 2D ($q = 0.7$), the maximum He band wave power occurs only at the last time interval (red curve). Similarly, H band wave power in Figure 2A ($q = 0.1$) does not grow appreciably until the second time interval (blue curve), but it is not observed in Figure 2B ($q = 0.3$) until the third time interval (green curve). Highest up on the field line in Figure 2D ($q = 0.7$), the H band power does not become appreciable even within the last time interval (red curve).

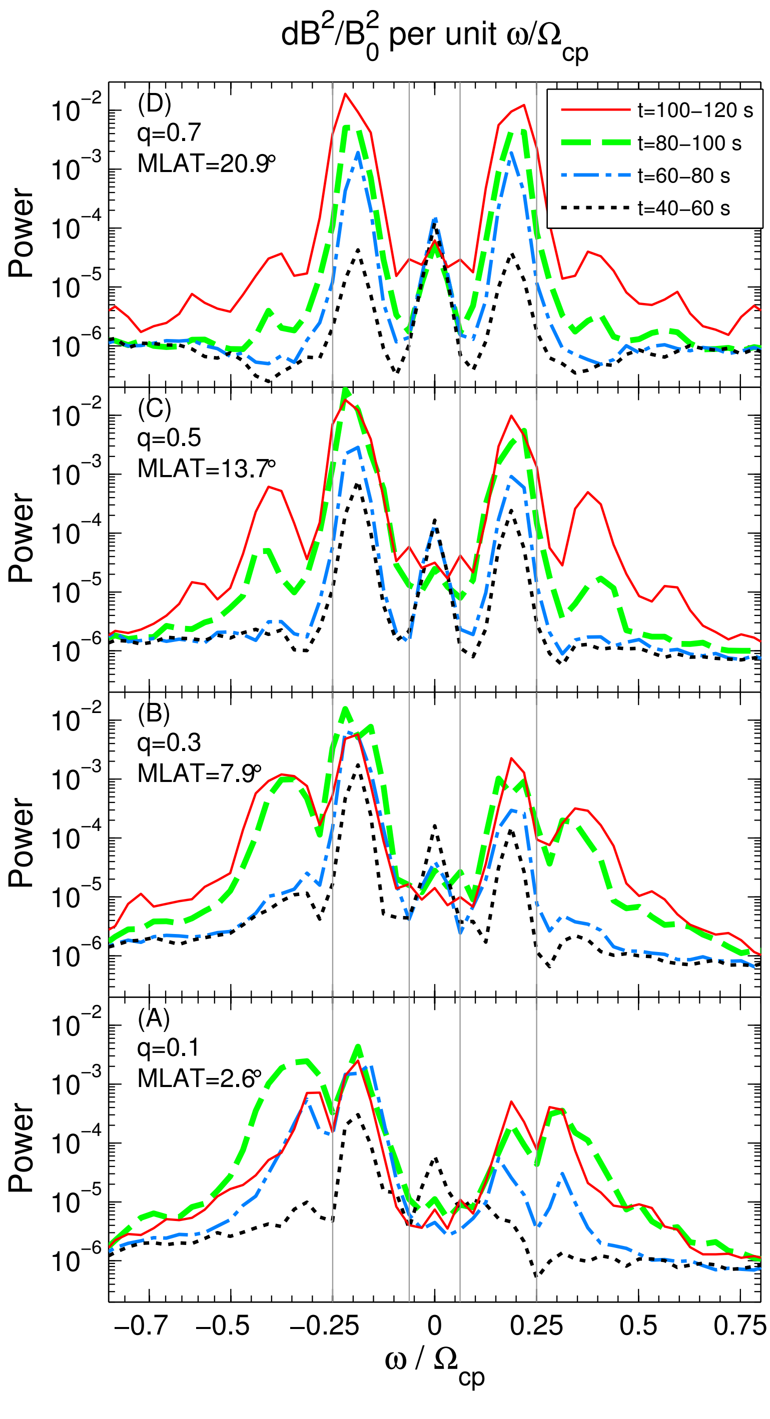

215 **Figure 2.** Wave power dB^2/B_0^2 per unit ω/Ω_{cp} versus ω/Ω_{cp} within the boxes of Figure 1 centered at (A) $q = 0.1$, (B) $q = 0.3$, (C) $q = 0.5$, and (D) $q = 0.7$. The dotted black, dash–dot blue, dashed green, and solid red curves show the wave power for the time intervals indicated in the legend of panel (D).

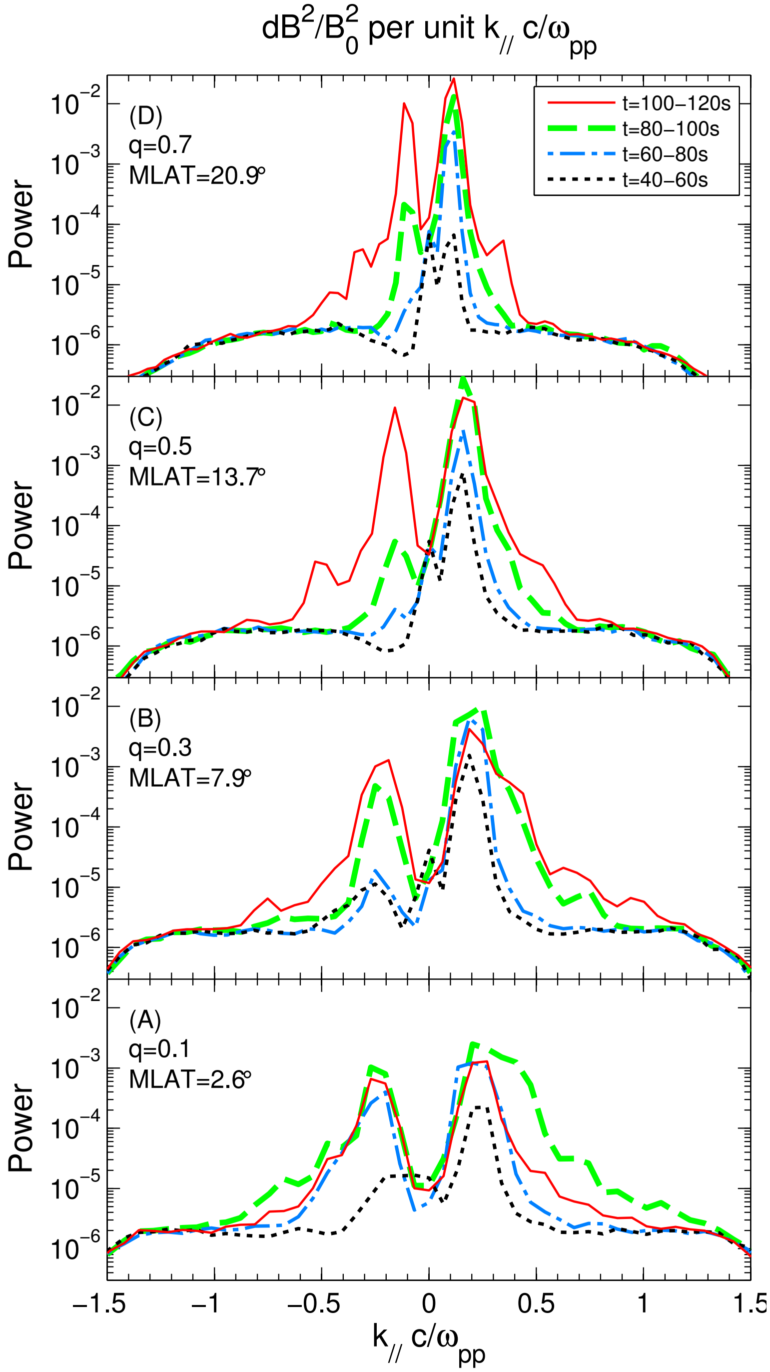

260 **Figure 3.** Wave power dB^2/B_0^2 per unit $k_{\|}c/\omega_{\mathrm{pp}}$ versus $k_{\|}c/\omega_{\mathrm{pp}}$ within the boxes of Figure 1 centered at
261 (A) $q = 0.1$, (B) q =0.3, (C) $q = 0.5$, and (D) $q = 0.7$. The dotted black, dash–dot blue, dashed green, and
262 solid red curves show the wave power for the time intervals indicated in the legend of panel (D).

3.2 $k_\parallel$ distribution

Figure 3 shows the wave power versus $k_\parallel c/\omega_{pp}$ in a format similar to that of Figure 2. Here the sign of $k_\parallel$ is chosen so that positive sign corresponds to waves propagating away from the magnetic equator, and negative sign corresponds to waves propagating toward the magnetic equator. (Assuming the functional form $\exp(i(\omega t - k_\parallel s))$, waves propagate in the positive s direction if the Fourier transformed $k_\parallel$, has the same sign as ω.) In general, there is a preference for waves propagating in the positive direction away from the magnetic equator; each peak at negative $k_\parallel$ in Figure 3 is smaller than the corresponding peak at positive $k_\parallel$. But there are some regions where significant wave growth in the negative direction occurs.

The time evolution of the $k_\parallel$ distribution of wave power is more complicated than that of the frequency. The initial waves (black curves) are strongly dominant in the positive direction, although there is some small growth with negative $k_\parallel$, especially at $q = 0.3$ (Figure 3B). (The early wave power overlapping $k_\parallel = 0$ may be associated with large-scale oscillations bringing the system into better equilibrium.) The wave power with positive $k_\parallel$ appears to grow in time while it propagates away from the magnetic equator. For instance, the black peak at $q = 0.1$ in Figure 3A may lead to the blue peak at $q = 0.3$ in Figure 3B, then to the green peak at $q = 0.5$ in Figure 3C, and finally to the red peak at $q = 0.7$ in Figure 3D. On the other hand, we would not expect the waves with negative $k_\parallel$ to propagate away from the magnetic equator. Two effects may explain the development of the wave power with negative $k_\parallel$. First of all, note that the peaks at $k_\parallel c/\omega_{pp} \sim -0.25$ first grow off the equator at $q = 0.3$ (black and blue curves in Figure 3B); then the negative $k_\parallel$ wave power at about that value of $k_\parallel c/\omega_{pp}$ appears later at $q = 0.1$ (blue, green, and red curves in Figure 3A). But there is also reflection of waves, as suggested by Figure 1Db. The reflection is presumably at the cutoff frequency and is discussed more in section 3.3 below.

The peaks in $k_\parallel$ shift to smaller values at larger q (comparing Figure 3D to Figure 3A). At least for the dominant He mode, this can be explained based on the alteration of the dispersion relation due to the larger off-equatorial magnetic field. This will be demonstrated more quantitatively in section 3.4.

3.3 Distribution of wave power versus $k_\parallel$ and ω

Figure 4 shows the distribution of wave power versus $k_\parallel c/\omega_{pp}$ on the horizontal axis and ω/Ω_{cp} on the vertical axis at the same times and positions as were used in Figure 2. Here, in order to show the different dispersion surfaces, six orders of magnitude of wave power are shown in each panel, with saturated color corresponding to the maximum wave power indicated next to the label in each panel. Blue color, green color, and red color correspond to left hand polarized, linearly polarized, and right hand polarized waves, as indicated by the color bar above Figure 4Da. Concentrating first on Figure 4Aa ($q = 0.1$ at $t = 40$–60 s), the blue regions represent the EMIC waves. The blue color at $\omega/\Omega_{cp} < 0.25$ is the He band, and the blue color between $\omega/\Omega_{cp} = 0.25$ and 1.0 is the H band; the red color at higher frequencies is the whistler mode [see also, e.g., *Ofman et al.*, 2017]. Since the whistler mode is stable and results from noise in the simulation, it is most prominent when the maximum wave power is small (comparing Figure 4Da to Figure 4Cc). Note that the H band extends to $\omega/\Omega_{cp} > 1$ farther from the magnetic equator (rows C and D). As mentioned in section 3.3, this is because the normalization is to Ω_{cp} at the normalization point, which is at the magnetic equator. Using the local gyrofrequency, the normalized frequency would be below unity as is normal for H band waves.

Figure 5 is similar to Figure 4 except that now the variation from white to saturated color represents linear variation from zero to the maximum power indicated next to the label in each panel. This plot accentuates the dominant wave power. As was noted in reference to Figures 2 and 3, the dominant wave power is in the He band with $k_\parallel > 0$ indi-

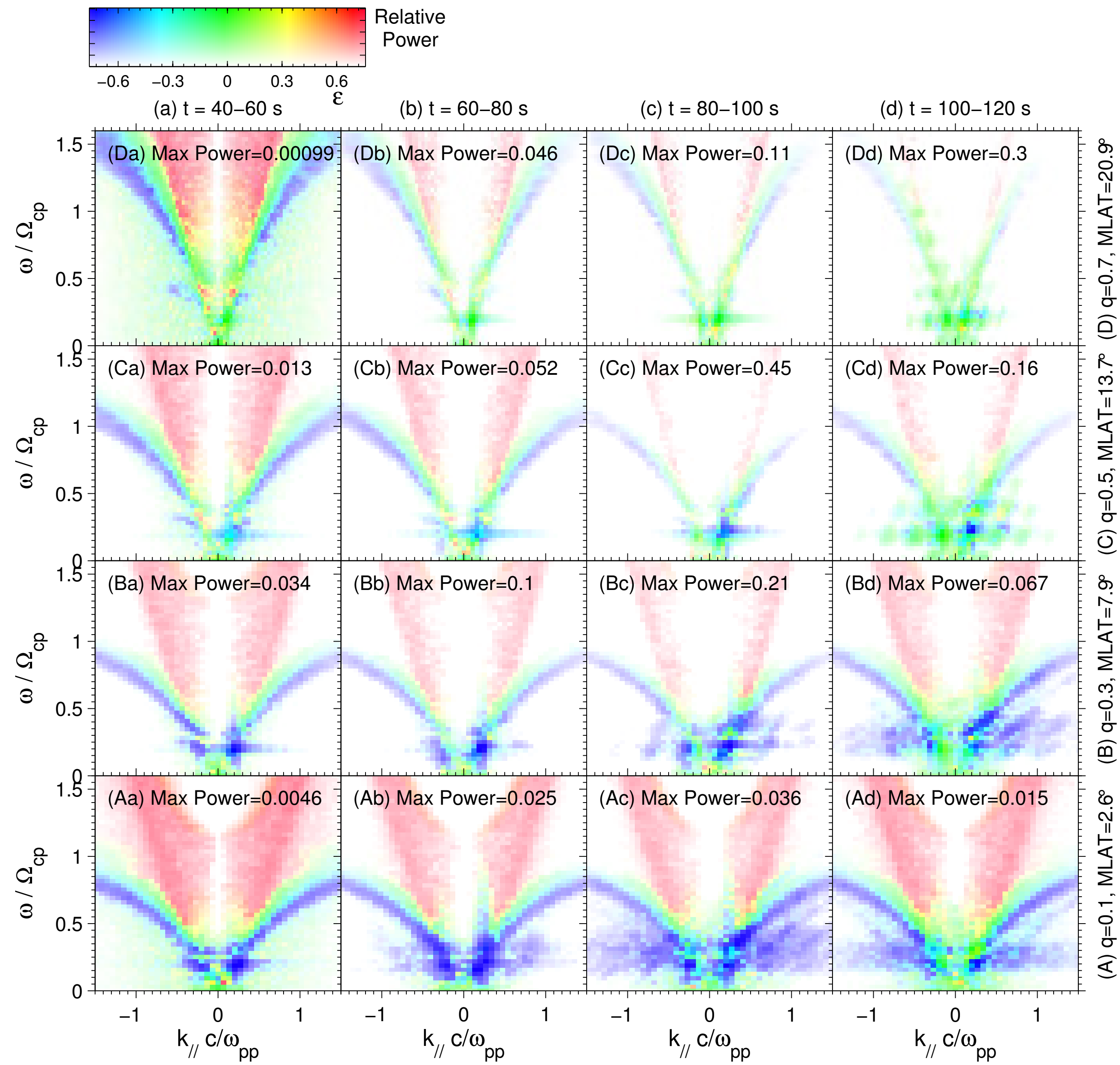

Figure 4. Wave power dB^2/B_0^2 per unit $(k_\parallel c/\omega_{\rm pp})(\omega/\Omega_{\rm cp})$ versus $k_\parallel c/\omega_{\rm pp}$ on the horizontal axis, and $\omega/\Omega_{\rm cp}$ on the vertical axis, at times (a) t = 40–60 s, (a) t = 60–80 s, (a) t = 80–100 s, and (a) t = 100–120 s, and within the boxes of Figure 1 centered at (A) q = 0.1, (B) q =0.3, (C) q = 0.5, and (D) q = 0.7. The color scale is different in each panel. The hue (particular color) indicates the ellipticity as indicated in the color bar above panel Da, but the variation from white to saturated color represents logarithmic variation with 6 orders of magnitude up to the maximum power indicated in each panel.

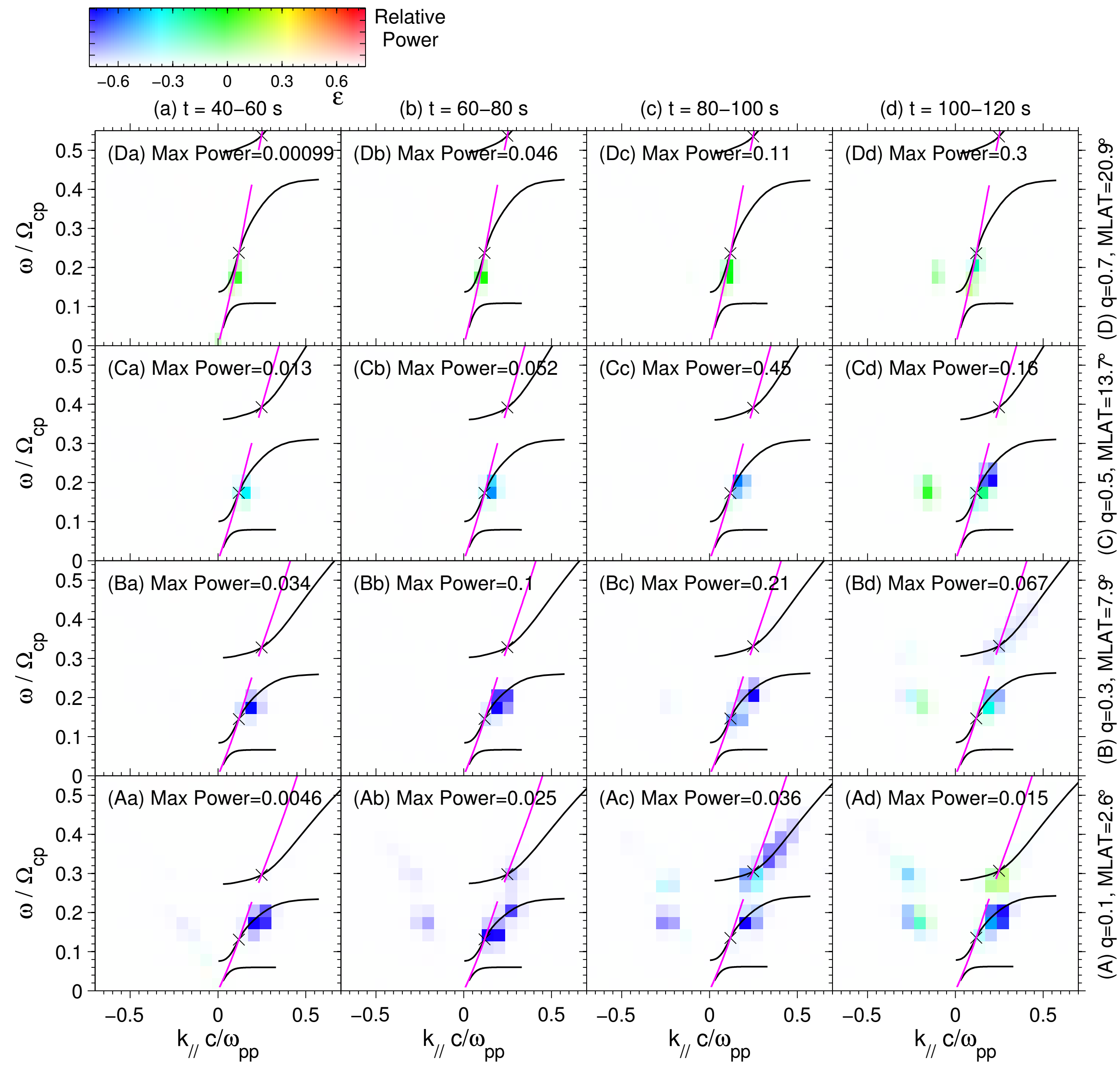

Figure 5. Wave power dB^2/B_0^2 versus $k_{\|}c/\omega_{\rm pp}$ and $\omega/\Omega_{\rm cp}$ like in Figure 5, except that here the variation from white to saturated color represents linear variation from zero to the maximum power indicated in each panel. The black curves are the linear dispersion surfaces for left-hand polarized waves and the magenta curves are the linear dispersion surfaces for right-hand polarized waves, both at nearly parallel propagation. The upper, middle, and lower curves are for the H band, He and, and O band waves. The black crosses mark the positions where the right hand polarized wave surfaces cross the left hand polarized surfaces.

cating propagation away from the magnetic equator. At t = 40–60 s, the maximum wave power is at q = 0.1; at t = 60–80 s, the maximum wave power is at q = 0.3; at t = 80–100 s, the maximum wave power is at q = 0.5; and at t = 100–120 s, the maximum wave power is at q = 0.7. At t = 60–80 s, some wave power in the H band starts to appear at q = 0.1 (Figure 5Ab). Observable H band wave power propagates to q = 0.3 by t = 100–120 s (Figure 5Bd). Wave power with negative $k_{\|}$ also begins to appear at t = 60–80 s (Figure 5Ab). As explained in section 3.2, this wave power might have propagated toward the magnetic equator from $q \sim 0.3$. At the final time, t = 100–120 s (column d), wave power with negative $k_{\|}$ appears also at other positions along the magnetic field line. The later occurrence probably results mostly from reflection, though there could be some local growth with smaller linear growth rate at high latitude.

Also shown in each panel of Figure 5 are the left hand polarized surfaces (black curves) for H band (upper black curves), He band (middle black curves), and O band (lower black curves) and right hand polarized services (magenta curves) for nearly parallel propagating waves propagating away from the magnetic equator (positive $k_{\|}$). The magenta curves would merge into a single curve for a cold plasma, but the numerical solutions for this plasma using WHAMP [*Ronnmark*, 1982, 1983] yielded discontinuous sections. Since the dispersion surfaces yield ω normalized to the local magnetic field, but the frequency in all the panels of Figure 5 (plotted on the vertical axis) is normalized to the equatorial magnetic field, we shift the equatorial dispersion relations up in frequency in the figure by the ratio of the local to equatorial magnetic field. We also show the position on the dispersion relations where the right hand polarized waves cross the left hand polarized waves as black crosses.

All of the observed waves lie close to the linear dispersion relations. As was noted earlier, the He band waves are the strongest. As the forward propagating He band waves propagate up to q = 0.7, the frequency of the waves is constant, and so is ω/Ω_{cp} because Ω_{cp} is the cyclotron frequency at the fixed equatorial normalization point. But if ω were normalized to the local gyrofrequency, its normalized frequency would decrease at larger MLAT. Alternately, the dispersion surfaces are rising relative to the fixed frequency of the waves. Then as the waves move down on the normalized dispersion surface, they also move to smaller $k_{\|}c/\omega_{pp}$. (The normalization factor for the wave vector, c/ω_{pp}, is not strongly dependent on latitude because the equilibrium cold density is constant along field lines.) This reduction in $k_{\|}c/\omega_{pp}$ is greatest at the larger latitudes where the local to equatorial magnetic field ratio is the largest. The local to equatorial magnetic field ratio is about 1., 1.1, 1.3, and 1.8 in Figure 5A, 5B, 5C, and 5C, respectively.

The He band waves become linearly polarized when the frequency approaches the crossover frequency (black crosses), as shown in Figure 5Cd and Dd. It is tempting then to consider the He mode wave power below the crossover frequency in Figure 5Dd to be on the right hand polarized surface. But, as mentioned in the Introduction, the left hand polarized surfaces seem to maintain the topology of the parallel propagating surfaces, even out to large oblique angles [see *Denton et al.*, 2014]. Thus if some wave power moves to the right hand polarized surface, it may be tunneling through to that surface from the left hand polarized surface. In any case, for large oblique angles, waves on either surface will tend to be linearly polarized.

The He band waves started to grow high up on their linear dispersion curve, and were thus able to continue to move down the locally normalized dispersion curve, even to q = 0.7. Because the dispersion curve is roughly linear in that regime, it explains the previously observed variation of $k_{\|}$, expected to be roughly proportional to $1/B$. The H band wave power, on the other hand, starts growing close to the crossover frequency and not far above the cutoff frequency (low $k_{\|}$ limit) of the left-hand polarized H mode (upper curve in Figure 5A). As explained by *Denton et al.* [2014], the normalized frequency of linearly unstable waves is limited by the anisotropy such that $\omega/\Omega_{\mathrm{cp,local}} < A/(A+1)$ (their equation 7), where $\Omega_{\mathrm{cp,local}}$ is the local proton gyrofrequency. For an anisotropy of 1, the normalized frequency must be less than 0.5. The result is that the He band waves can be driven on the high-frequency part of their dispersion curve, but the H band waves must be driven on the low-frequency part of their dispersion curve. Therefore there is not much room for the H band waves to travel down the locally normalized dispersion surface before reflecting at the cutoff frequency; H band waves are strongest at $q = 0.1$ and $q = 0.3$ (Figure 5A and 5B). Within this range of MLAT, B does not vary greatly (only by 1.1 to $q = 0.3$), so not much variation is seen in $k_\parallel$ for the H band waves.

3.4 Latitudinal dependence of dominant wave

Now we plot in Figure 6 the properties of the dominant waves propagating away from the magnetic equator ($k_\parallel > 0$). At each time and latitude (q), we calculate the total wave power and the power weighted $k_\parallel$ and ϵ for the He and H wave bands. The results are shown in Figure 6. The strongest wave power is slightly less than $2 \times 10^{-3} B_0^2$ in the He band at $q = 0.5$ (green curve in Figure 6Aa). This implies a wave amplitude of roughly $\sqrt{2 \times 10^{-3}} = 0.045 B_0$ normalized to the equatorial magnetic field, or $0.04/1.3 = 0.03$ normalized to the local magnetic field at $q = 0.5$. This is a large but not unrealistic value.

Consider first the wave power in the He band (Figure 6a). Initially, the wave power is strongest off the magnetic equator at $q = 0.3$ (blue curve in Figure 6Aa); but later, at $t = 90$ s, the strongest wave power is at $q = 0.5$ (green curve); and at the last time plotted, $t = 110$ s, the strongest wave power is at $q = 0.7$ (red curve). This implies propagation of the wave power away from the magnetic equator, as we have already discussed. The He wave power at $q = 0.7$ appears still to be growing (red curve in Figure 6a), so it might rise at later times to slightly higher values than the highest values at $q = 0.5$ (green curve). The power weighted value of $k_\parallel$ decreases at larger q (comparing the different curves in Figure 6Ba), consistent with Figures 3 and 5. But when we multiply $k_\parallel$ by B/B_0 (Figure 6Ca), the resulting product is almost invariant. This demonstrates the $k_\parallel \propto 1/B$ scaling that we discussed in section 3.3. The power weighted ellipticity (Figure 6Fa) is more negative (more left-handed) close to the magnetic equator at $q = 0.1$, and is close to zero, indicating linear polarization, at $q = 0.7$. The ellipticity at $q = 0.1$ is most negative at the earliest time, and farther away from the magnetic equator the ellipticity is most negative when the strongest wave power propagates up to that position from close to the magnetic equator. For instance, the ellipticity is most negative at $q = 0.7$ at $t = 110$ s when the wave power reaches a maximum at that position.

Now consider the wave power in the H band (Figure 6b). In this case, the wave power never becomes large at $q = 0.7$ (red curve in Figure 6Ab), and the wave power at $q = 0.5$ (green curve in Figure 6Ab) only becomes larger than that at $q = 0.1$ (black curve in Figure 6Ab) at the end of the simulation when the wave power at $q = 1$ drops significantly. As we saw from Figure 5, the wave power in the H band generated near the magnetic equator is not able to propagate to $q = 0.7$ because at that latitude the normalized wave frequency of the equatorially generated waves has decreased below the cutoff frequency. Therefore the H band wave power observed at $q = 0.7$ must be generated locally. While some of the higher frequency portion of the H band wave power generated equatorially may be able to propagate to $q = 0.5$ (if ω/Ω_{cp} is at least as great as 0.36; see Figure 5C), the strongest wave power generated equatorially in the H band has lower frequency (see Figure 5Ac) and will not be able to propagate to $q = 0.5$. For this reason, the waves in the H band observed at $q = 0.5$ are either locally generated waves with higher frequency or waves that have propagated away from the magnetic equator, but limited to the higher frequencies. In either case, the higher frequency waves are associated with higher $k_\parallel$. For this reason, the power averaged $k_\parallel$ is not $\propto 1/B$ (Figure 6Cb) like it was for the He band because the dominant waves observed close to the magnetic equator are not the same waves that are observed at $q \geq 0.5$. Rather the wave power averaged $k_\parallel$ is almost constant with respect to q (Figure 6Bb). Like we saw for the He band, the power weighted ϵ becomes closer to zero at larger q. The values of ϵ are a little closer to

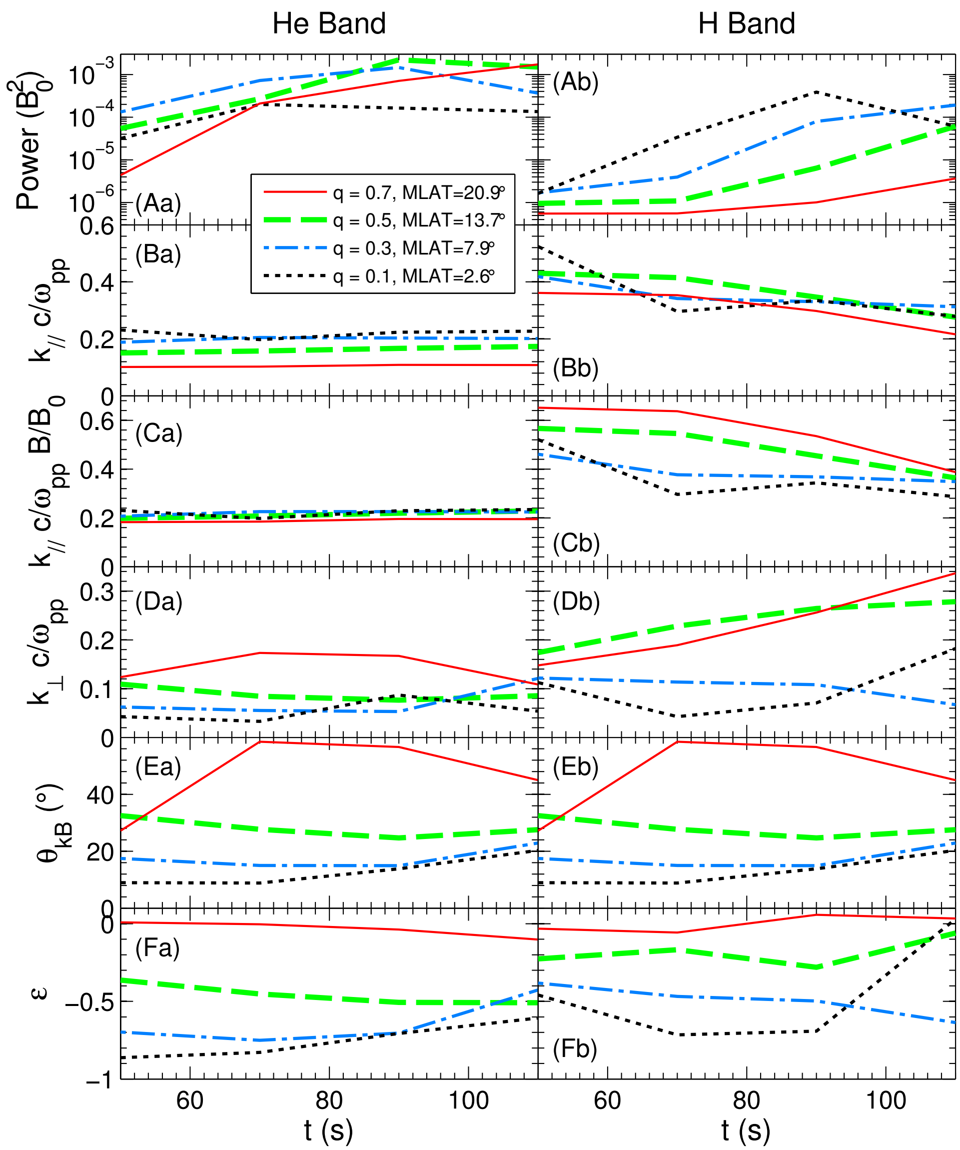

Figure 6. Properties of the dominant wave propagating away from the magnetic equator. (A) The total wave power, (B) power weighted $k_\parallel c/\omega_{pp}$, (C) power weighted $k_\parallel c/\omega_{pp} B/B_0$, (D) power weighted $k_\perp c/\omega_{pp}$, (E) wave normal angle θ_{kB} based on the power weighted **k** from B and D, and (F) power weighted ϵ for (a) the He band and (b) H band, versus time t. The normalization uses quantities at the magnetic equator on the central field line.

zero for the H band compared to the He B band, possibly because the H band waves are generated lower in relative frequency on their wave band or because they are not as well developed (smaller amplitude).

3.5 $k_\perp$ dependence

Figure 7 shows the distribution of wave power with respect to $k_\perp$ with respect to time (different curves) and position along the field line (different panels). Note that the precipitous drop in wave power at large $k_\perp$ is due to the low pass filtering to eliminate grid scale waves. As was the case for $k_\|$, positive $k_\perp$ corresponds to propagation in the positive L direction. At the earliest time close to the magnetic equator (black curve in Figure 7A), the peak in the distribution is close to $k_\perp = 0$ and the peak is relatively narrow. The central value of the peak and the width of the distribution both increase with increasing time and q. On the other hand, the peaks in $k_\|$ decrease at large q, at least for the dominant He band waves, due to the motion of the locally normalized wave frequency down the dispersion relation, as discussed in section 3.3. These opposite trends coordinate with the turning of the wave fronts to become more oblique at large q.

Figure 6, discussed in section 3.4, shows the wave power weighted $k_\perp c/\omega_{pp}$ (Figure 6D) and wave normal angle $\theta_{kB} = \tan^{-1}(k_\perp/k_\|)$ (Figure 6E) using the wave power weighted values of $\mathbf{k}$ for He band (Figure 6a) and H band (Figure 6b) waves propagating away from the magnetic equator ($k_\| > 0$). Because the waves refract outward as they propagate away from the magnetic equator [*Denton et al.*, 2014], the values of $k_\perp c/\omega_{pp}$ and θ_{kB} are larger farther away from the magnetic equator (comparing, e.g., the red curves in Figure 6D and E to the black curves).

Figure 8 shows the wave power distribution for the He band waves versus $k_\| c/\omega_{\rm pp}$ and $k_\perp c/\omega_{\rm pp}$ within the boxes of Figure 1 at four different locations along the field line in the four time intervals studied in this paper. Similarly, Figure 9 shows the same information, but for the H band waves. These plots show many features already mentioned, the transition to linear polarization, the decrease in $k_\|$, and the broadening and shift of $k_\perp$ to more positive values at large q. Figures 8 and 9 also show that $k_\perp$ shifts to more positive values (outward propagation) for negative as well as positive $k_\|$.

3.6 Data files

In the Supplementary Information file, we describe data files for this paper. These include time-dependent values of the q, r, and s components of the magnetic and electric field (data set ds01); the instantaneous parallel, L, and s components of the magnetic and electric field at the four times shown in Figure 1 (ds02); and the Fourier transformed magnetic and electric field within the boxes of Figure 1 using the four time intervals studied in this paper (ds03).

4 Summary

We have examined in detail the evolution of electromagnetic ion cyclotron (EMIC) waves in an approximately dipole magnetic field for one particular case. The cold density is relatively high representing a plasmasphere or plume-like plasma at geostationary orbit, and the temperature anisotropy of the hot protons, $A = T_{\perp,\rm hot}/T_{\|,\rm hot}$ is limited to unity. The parameters vary in space such that the most unstable conditions are near the magnetic equator on the central field line.

The two main effects of the dipole geometry are curvature, which causes radially outward turning of the wave vector [*Denton et al.*, 2014], and the increase in the equilibrium magnetic field at high latitude, which alters the dispersion relations.

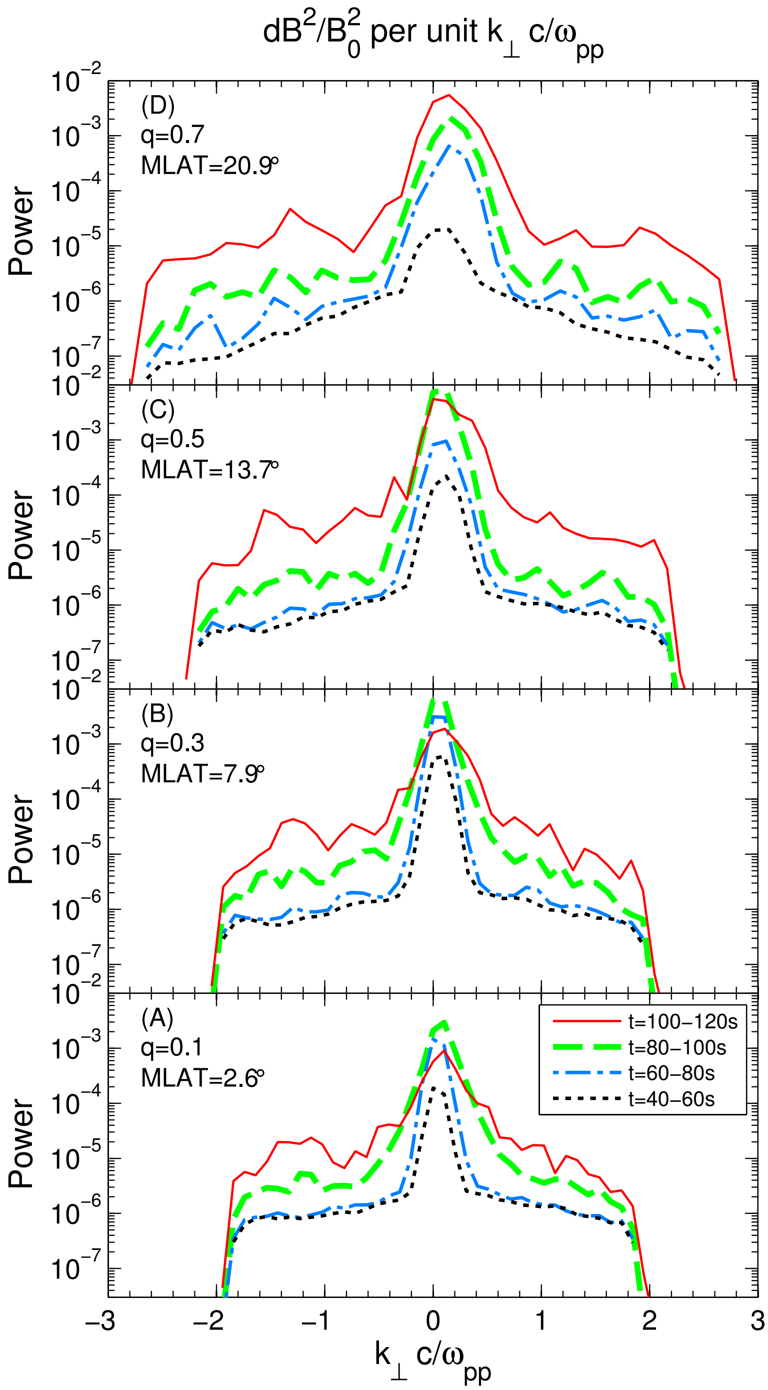

Figure 7. Wave power dB^2/B_0^2 per unit $k_\perp c/\omega_{\rm pp}$ versus $k_\perp c/\omega_{\rm pp}$ within the boxes of Figure 1 centered at (A) $q = 0.1$, (B) $q = 0.3$, (C) $q = 0.5$, and (D) $q = 0.7$. The dotted black,dash–dot blue, dashed green, and solid red curves show the wave power at the times indicated in the legend of panel (A).

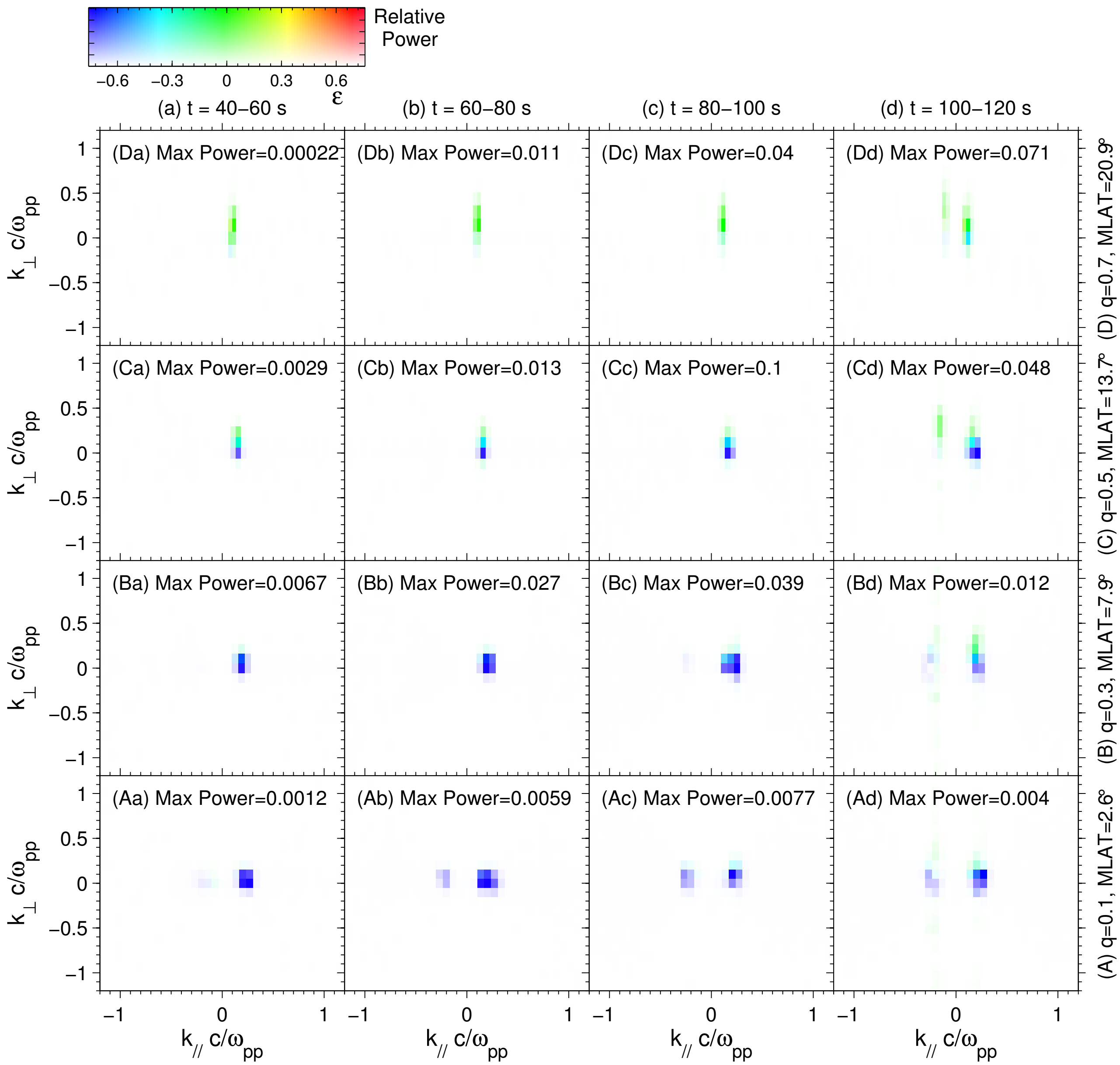

Figure 8. Distribution of wave power $(dB/B_0)^2$ versus $k_\parallel c/\omega_{pp}$ on the horizontal axis and $k_\perp c/\omega_{pp}$ on the vertical axis per unit $k_\parallel k_\perp (c/\omega_{pp})^2$ for the He wave band within the boxes of Figure 1 centered at (A) $q = 0.1$, (B) $q = 0.3$, (C) $q = 0.5$, and (D) $q = 0.7$, for (a) $t = 40$–60 s, (b) $t = 60$–80 s, (c) $t = 80$–100 s, and (d) $t = 100$–120 s. In each panel, the wave power is plotted with a linear scale, where white represents zero wave power, and saturated color is the maximum power listed next to each panel label. The hue, or particular color, represents the ellipticity, as shown in the color scale above Figure 8Da

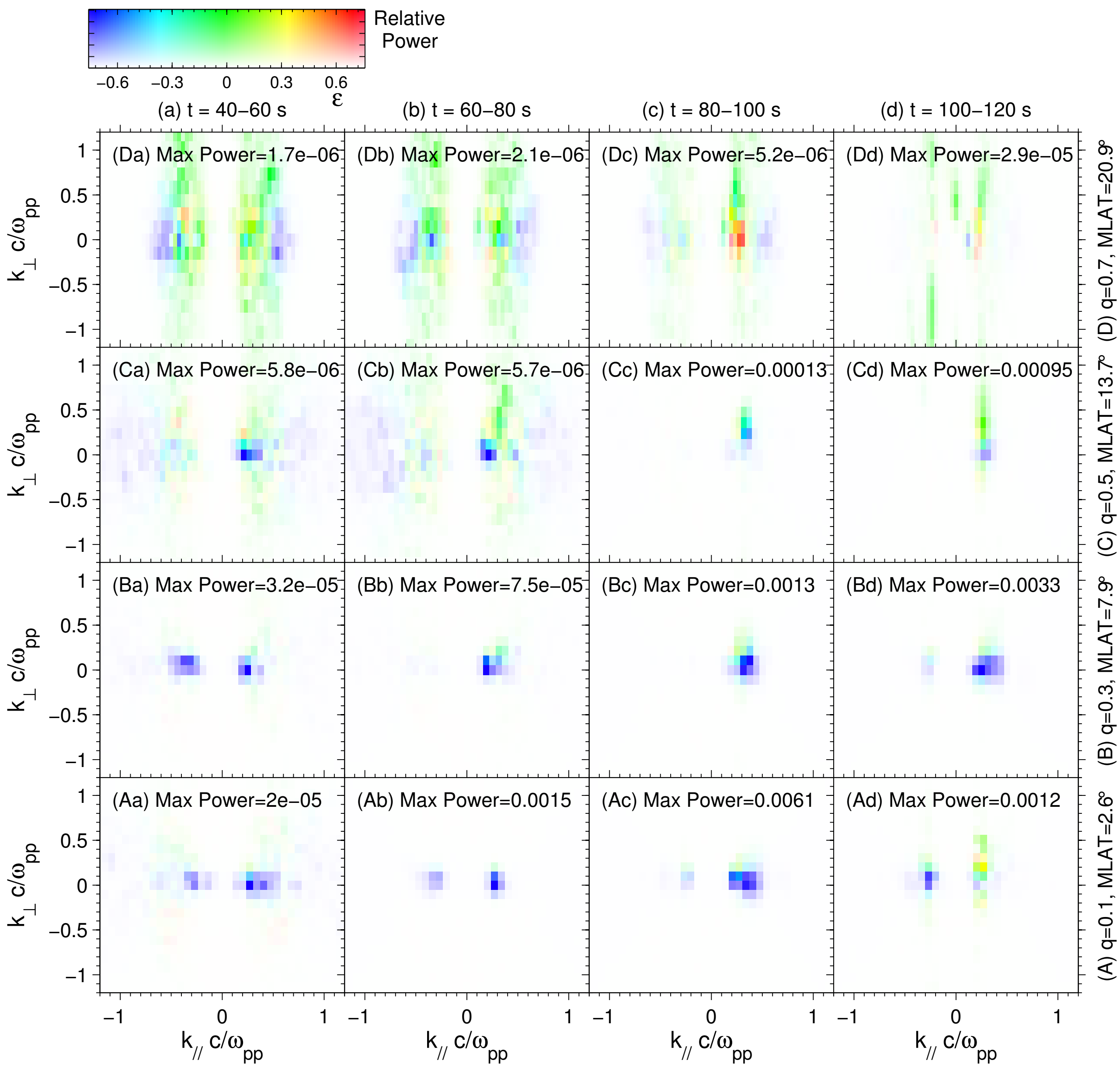

466 **Figure 9.** Similar to Figure 8, except showing the wave power distribution of the H band waves.

Waves grow out of the numerical noise near, but not exactly at, the magnetic equator. If the symmetry boundary condition at the magnetic equator were relaxed, waves might grow there [*Hu and Denton*, 2009]. As the waves propagate along magnetic field lines away from the magnetic equator, they grow and their wave vector turns radially outward, leading to linear polarization at the higher latitudes. The strongest waves propagate away from the magnetic equator, but some wave power propagating toward the magnetic equator is observed due to local generation (especially close to the magnetic equator) and reflection at high latitudes. Since we don't have parallel electric field in the simulation, there is no Landau damping and the growth of oblique waves is likely overestimated.

By examining the wave power in limited regions, we were able to calculate the wave vector of the waves and show how the waves move down their dispersion surface. The H band waves experienced a frequency filtering effect. Only higher frequency waves could propagate to high latitudes because the lower frequency waves were reflected when the locally normalized wave frequency decreased to the H band cut-off frequency. This effect also occurs for the He band waves, but at higher latitude than where we calculated the wave properties. Within the range of MLAT that we considered, $0°$ to $21°$, the wave power averaged $k_\parallel$ was roughly proportional to the inverse of the local magnetic field for the He band waves, consistent with their motion along the dispersion relation. But the wave power averaged $k_\parallel$ of the H band waves was almost constant because of the frequency filtering (see section 3.4). At the same time that $k_\parallel$ decreased for the He band waves, the central value of $k_\perp$ increased and the peak broadened for both wave bands.

The wave fields that we have simulated should be useful for quasi-linear and test particle simulations of radiation belt particle dynamics. In this simulation, the dominant H band waves have slightly larger $k_\parallel$ than the dominant He band waves, and some H band wave power extends to significantly higher frequency with correspondingly higher $k_\parallel$ (Figure 5Ac). This is in disagreement with equation (7) of *Denton et al.* [2015], who assume that waves in both He and H bands are in resonance with hot protons having parallel velocity equal to the hot proton parallel thermal velocity. Apparently the H band waves are driven by lower velocity protons than are the He band waves. (Note that in the simulation of *Denton et al.* [2014] used by *Denton et al.* [2015], the H band waves did not appear in the same spatial region as the He band waves; and *Denton et al.* [2015] examined only the dominant waves.) The result is that in this case the minimum resonant energy of radiation belt electrons will be lower for interaction with the H band waves, especially with the higher frequency H band waves.

Acknowledgments

Work at Dartmouth College was supported by NASA grant NNX13AD65G. The data from the simulation is available online as discussed in section 3.6.

References

Andre, M. (1985), Dispersion surfaces, *Journal of Plasma Physics*, *33*(FEB), 1–19.

Arfken, G. (1970), *Mathematical Methods for Physicists*, 2nd ed., Academic Press, New York.

Birdsall, C. K., and A. B. Langdon (1985), *Plasma physics via computer simulation*, McGraw-Hill, New York.

Denton, R. E., V. K. Jordanova, and B. J. Fraser (2014), Effect of spatial density variation and O+ concentration on the growth and evolution of electromagnetic ion cyclotron waves, *J. Geophys. Res.*, *119*(10), 8372–8395, doi:10.1002/2014ja020384.

Denton, R. E., V. K. Jordanova, and J. Bortnik (2015), Resonance of relativistic electrons with electromagnetic ion cyclotron waves, *Geophys. Res. Lett.*, *42*(20), 8263–8270, doi: 10.1002/2015gl064379.

Fraser, B. J., T. M. Loto'aniu, and H. J. Singer (2006), Electromagnetic ion cyclotron waves in the magnetosphere, in *Magnetospheric Ulf Waves: Synthesis and New Directions*, *Geophysical Monograph Series*, vol. 169, edited by K. Takahashi, P. J. Chi, R. E. Denton, and R. L. Lysak, pp. 195–212, times Cited: 27 Chapman Conference on Magnetospheric ULF Waves Mar 21-25, 2005 San Diego, CA Nasa; nsf.

Hu, Y. (2010), Hybrid code simulation of electromagnetic ion cyclotron waves in curvilinear coordinates, (Ph.D. dissertation), Hanover, NH: Dartmouth College, Ph.D. thesis.

Hu, Y., and R. E. Denton (2009), Two-dimensional hybrid code simulation of electromagnetic ion cyclotron waves in a dipole magnetic field, *J. Geophys. Res.*, *114*, doi: 10.1029/2009ja014570.

Hu, Y., R. E. Denton, and J. R. Johnson (2010), Two-dimensional hybrid code simulation of electromagnetic ion cyclotron waves of multi-ion plasmas in a dipole magnetic field, *J. Geophys. Res.*, *115*, a09218, doi:10.1029/2009ja015158.

Johnson, J. R., and C. Z. Cheng (1999), Can ion cyclotron waves propagate to the ground?, *Geophys. Res. Lett.*, *26*(6), 671–674, doi:10.1029/1999gl900074.

Kodera, K., R. Gendrin, and C. Devilledary (1977), Complex representation of a polarized signal and its application to analysis of ULF waves, *J. Geophys. Res.*, *82*(7), 1245–1255, doi:10.1029/JA082i007p01245.

Kubota, Y., Y. Omura, and D. Summers (2015), Relativistic electron precipitation induced by EMIC-triggered emissions in a dipole magnetosphere, *J. Geophys. Res.*, *120*(6), 4384–4399, doi:10.1002/2015ja021017.

Liu, K., D. S. Lemons, D. Winske, and S. P. Gary (2010a), Relativistic electron scattering by electromagnetic ion cyclotron fluctuations: Test particle simulations, *J. Geophys. Res.*, *115*, a04204, doi:10.1029/2009ja014807.

Liu, K., S. P. Gary, and D. Winske (2010b), Spectral properties of the Alfven cyclotron instability: Applications to relativistic electron scattering, *J. Geophys. Res.*, *115*, a08212, doi:10.1029/2009ja015201.

Lui, A. T. Y., R. W. McEntire, and S. M. Krimigis (1987), Studies of storm-time ring current from the AMPTE-CCE MEPA measurements, *Physica Scripta*, *36*(2), 378–381, doi:10.1088/0031-8949/36/2/031.

Millan, R. M., and R. M. Thorne (2007), Review of radiation belt relativistic electron losses, *J. Atmos. Sol.-Terr. Phys.*, *69*(3), 362–377, doi:10.1016/j.jastp.2006.06.019.

Ofman, L., R. E. Denton, J. Bortnik, X. An, A. Glocer, and C. Komar (2017), Growth and nonlinear saturation of electromagnetic ion cyclotron waves in multi-ion species magnetospheric plasma, *J. Geophys. Res.*, *122*(6), 6469–6484, doi:10.1002/2017ja024172.

Omura, Y., and Q. Zhao (2012), Nonlinear pitch angle scattering of relativistic electrons by EMIC waves in the inner magnetosphere, *J. Geophys. Res.*, *117*, a08227, doi: 10.1029/2012ja017943.

Omura, Y., and Q. Zhao (2013), Relativistic electron microbursts due to nonlinear pitch angle scattering by EMIC triggered emissions, *J. Geophys. Res.*, *118*(8), 5008–5020, doi:10.1002/jgra.50477.

Press, W. H., B. P. Flannery, S. A. Teukolsky, and W. T. Vetterling (1986), *Numerical Recipes*, Cambridge Univ. Press, New York.

Ronnmark, K. (1982), Waves in homogeneous, anisotropic, multicomponent plasmas, *Tech. Rep. Kiruna Geophys. Inst. Rep. 179, 56 pp.*, Swedish Institute of Space Physics, Univ. of Umea, Sweden.

Ronnmark, K. (1983), Computation of the dielectric tensor of a maxwellian plasma, *Plasma Physics and Controlled Fusion*, *25*(6).

Shprits, Y. Y., D. A. Subbotin, N. P. Meredith, and S. R. Elkington (2008), Review of modeling of losses and sources of relativistic electrons in the outer radiation belt. ii: Local acceleration and loss, *J. Atmos. Sol.-Terr. Phys.*, *70*(14), 1694–1713, doi: 10.1016/j.jastp.2008.06.014.

Summers, D., B. Ni, and N. P. Meredith (2007), Timescales for radiation belt electron acceleration and loss due to resonant wave-particle interactions: 1. theory, *J. Geophys.*

594 *Res.*, *112*(A4), doi:10.1029/2006JA011801.